Velocity and current measurements in electroconvecting smectic films

Stephen W. Morris*
Department of Physics, University of Toronto, 60 St. George Street, Toronto, Ontario, Canada M5S 1A7

John R. de Bruyn
Department of Physics, Memorial University of Newfoundland, St. John's, Newfoundland, Canada A1B 3X7

A. D. May
Department of Physics, University of Toronto, 60 St. George Street, Toronto, Ontario, Canada M5S 1A7
and Ontario Laser and Lightwave Research Centre, 60 St. George Street, Toronto, Ontario, Canada M5S 1A7
(Received 15 July 1991)

We have studied electrically driven convective flow in thin, freely suspended films of smectic-*A* liquid crystal. Here we report measurements of the two-dimensional velocity field of this flow as the driving voltage is varied. Our results are well described by the first few terms of an appropriate mode expansion over a range of the experimental control parameter, from the onset of convection to the appearance of unsteady flow substantially above onset. The behavior of the mode amplitudes near onset indicates that the bifurcation to convection is forward. We also present measurements of the current through the film, which show an enhanced charge transport due to convection, and measurements of the pattern wavelength at and above onset. We argue that a reduction in the onset wavelength observed above a cutoff frequency is related to the relaxation time of the charge distribution in the film.

PACS number(s): 47.65.+a, 61.30.−v

I. INTRODUCTION

Extended nonlinear dissipative systems exhibit progressively more complex spatial and temporal patterns as they are driven further and further out of equilibrium by externally imposed stresses. Rayleigh-Bénard convection is perhaps the best known example [1–4]; other well-studied fluid-dynamical systems include Taylor-Couette flow [1,5], and electroconvection in nematic liquid crystals [6,7]. In these systems, the experimental boundary conditions and the physical properties of the working fluid are well known and well controlled, allowing close contact with theoretical work. As the general three-dimensional case is rather complex, it is interesting to consider systems in which constraints due to boundary conditions or symmetry considerations lead to simple patterns. In previous publications [8–10], we have reported on experimental studies of the onset of pattern-forming flow in a new system—electroconvection in a thin, freely suspended film of smectic liquid crystal. As described elsewhere [10], the unique properties of the smectic phase constrain the film to behave as an isotropic, two-dimensional fluid. A simple two-dimensional, steady-flow pattern occurs in the film when a large enough electric field is applied in the plane of the film. This pattern becomes unsteady at higher applied voltages. In this paper, we present further results concerning the onset of convection in this system, as well as measurements of the convective velocity field in the steady-flow regime.

Smectic liquid crystals are highly anisotropic materials in which orientationally ordered long molecules arrange themselves into layers [11,12]. Our experiments were performed on a smectic-*A* material, in which the long axis of the molecules is perpendicular to the plane of the layers. In this phase, the liquid crystal behaves like an isotropic liquid for flows in the layer plane, but like a plastic crystal for flows perpendicular to the layers [12–14]. Smectic liquid crystals very easily form stable, freely suspended films, containing an integer number of smectic layers [15]. Such a film, which is supported only at its edges, can behave as a nearly ideal two-dimensional liquid. A substantial body of work has explored the structure and thermodynamics of smectic films [15–18], particularly those of the smectic-*C* phase, in which the molecules are tilted with respect to the layer normal. While molecular alignment due to flow has been observed in smectic-*C* films [19], our experiments are the first to take full advantage of the two-dimensional nature of smectic films for the study of hydrodynamic stability. The hydrodynamic flow we observe in our smectic-*A* films does not involve molecular reorientation and need not cause changes in the film thickness [9,10].

The behavior of smectic films may be contrasted with that of soap films, on which a number of hydrodynamic experiments have been performed [20–23]. A soap film is essentially a water film stabilized by monolayers of soap molecules on its free surfaces. The behavior of a flowing soap film is rather complex [22] due to internal motions, thickness changes, and variations in surface tension. Soap films are also somewhat difficult to handle experimentally because they drain rather rapidly and lose water by evaporation. Smectic liquid crystals, on the other hand, are nearly pure materials with no significant vapor pressure. Smectic films can flow without deformation of the free surfaces and hence without changes in surface

 ©1991 The American Physical Society

tension. Internal flows which would cross smectic layers are strongly suppressed by the structure of the film. Smectic films are therefore much closer to ideal two-dimensional incompressible fluids than soap films, and their dynamical behavior should therefore be of some interest.

Our experimental apparatus has been described elsewhere [9,10]. Briefly, it consisted of a rectangular smectic-A film suspended between two 15-μm electrode wires and two thin glass wipers used to draw the film, as shown in Fig. 1. The long edges of the film were supported by, and in contact with, the electrodes, while the wipers supported the ends. The length L and width d of the film were adjustable; in most of our experiments, $L \approx 20$mm and $d \approx 2$ mm. We have also observed similar convective flow in annular films suspended between electrodes in the form of concentric circular knife edges [10].

The material used in this work was 4,4′−n−octylcyanobipheyl (8CB) doped with 7.5±0.2 mM/l tetracyanoquinodimethane (TCNQ) to control the nature of ionic species present in the liquid crystal [10,24]. The films in which convection was studied had a uniform thickness of between 20 and a few hundred smectic layers, where the layers have a thickness of 3.16 nm [25]. Since these films are on the order of one wavelength of visible light thick, they show brilliant interference colors when observed under reflected white light. A change in film thickness of a single layer is observable by eye as a change in the film color; thus the uniformity of the film thickness can be determined to within a single layer from the uniformity of the film color. If some care is taken to avoid excess liquid crystal on the electrodes and wipers at the edges of the film, an initially uniform film can be driven into very rapid convection without thickness change. This is a unique feature of the smectic phase, in which the layer structure constrains the flow to remain in the plane of the layers. The film thickness s was determined with single-layer resolution from measurements of the reflectivity of the film at six wavelengths of an argon ion laser [10,26,27]. Flow visualization was accomplished by dusting the film with fine powder and illuminating it with the laser; the motion of the flow visualization particles was observed with a low-power microscope [10].

In our previous work [9,10] we discussed some characteristics of this system close to the onset of convection, which we briefly summarize here. Below a critical voltage V_c, there is no flow. At V_c steady convective flow begins; within the resolution of our visual determination of V_c the onset is nonhysteretic. The flow pattern consists of a series of vortices of alternating vorticity; the wavelength of the pattern in the x direction (see Fig. 1) is equal to $(1.30\pm0.05)d$. At a higher voltage, on the order of $5V_c$, a transition to unsteady flow occurs. With a dc applied field, the wavelength of the pattern is independent of voltage up to this transition.

With an ac applied voltage the flow periodically reverses direction at the applied frequency. The peak velocity of the reversing flow increases as the voltage is increased above onset. The critical voltage increases with both frequency and the film thickness s. V_c also increases with, but is not proportional to, d, as shown in Fig. 2. The wavelength of the pattern at onset retains its dc value up to a frequency ω', above which the wavelength decreases continuously until at frequencies $\omega \gg \omega'$ the pattern at onset consists of two lines of small vortices localized along the two electrodes. This change in the pattern appears to be a consequence of the finite relaxation time of the charge distribution, as discussed below. As the voltage is increased above onset at frequencies above ω', the pattern wavelength gradually increases to its dc value [10].

The remainder of this paper is organized as follows. In Sec. II we write down and discuss the electrohydrodynamic equations relevant to this system. A stability analysis of these equations is beyond the scope of this paper; our purpose in Sec. II is to make clear the mechanisms of charge creation in the film and to suggest directions for future theoretical work. In Sec. III we present our experimental results, beginning with measurements of the current-voltage characteristics of the films. These data provide information about the degree to which the film can be described as an Ohmic conductor. The decrease of the pattern wavelength with frequency is examined next, and explained qualitatively as a consequence of exceeding the relation frequency of the charge distribution in the film. Finally, we present measurements of the complete flow velocity field as a function of applied volt-

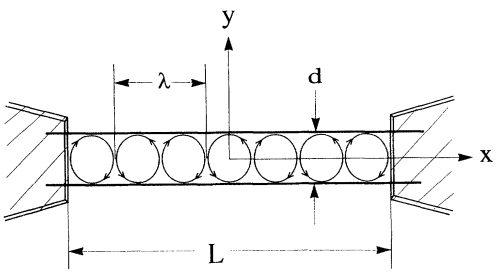

FIG. 1. A schematic view of the film holder, showing the coordinate axes, the length L and width d of the film and the wavelength λ of the vortex pattern.

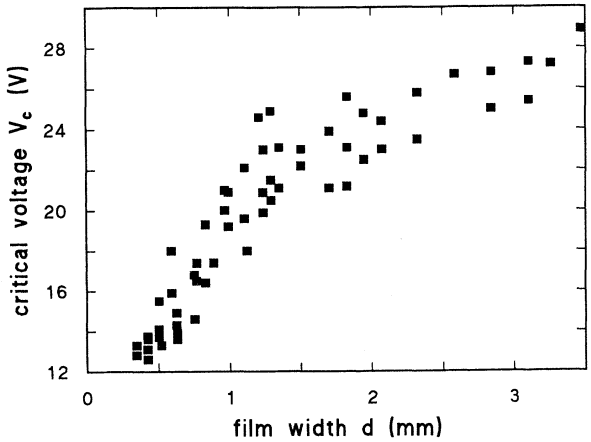

FIG. 2. The critical voltage at dc as a function of film width for a film of thickness 107±2 layers.

age. The modal structure of the flow field is obtained by a fit to an expansion in terms of eigenfunctions relevant to our geometry and boundary conditions. The voltage dependence of the amplitudes of the various modes has the form expected for a forward bifurcation when the dimensionless stress parameter is chosen to be quadratic in the applied voltage. Section IV is a brief discussion of our results and future prospects for study of this system.

II. EQUATIONS OF MOTION

In this section we write down the electrohydrodynamical equations pertaining to this system. Similar systems of equations have been derived for a variety of electroconvecting systems [28–34], and in some special cases linear and nonlinear stability analyses have been carried out. In this section we attempt a very general discussion intended to clarify the mechanism of the convection and to serve as a basis for discussion of our observations. A complete stability analysis should be possible for our system, but for the present we content ourselves with some suggestions as to how one might proceed.

The body force responsible for the fluid motion in our films is due to an electric field acting on regions of nonzero space-charge density, which arise due to spatial separation of ions dissolved in the liquid crystal [12]. Charge may be transported by a combination of migration, diffusion, and convection. The mobility and diffusion coefficient of liquid crystals are anisotropic in general, and in certain nematics these anisotropies are responsible for the creation of space charge, and hence convection [6,7,11,12]. Our observation that the alignment of the smectic molecules does not change under convection indicates that this process cannot be relevant to our case. We therefore treat the mobility and diffusion coefficient as scalars. Typical values of these properties, which we use in our discussion, are [35] $\mu \sim 10^{-10}$ m^2/Vs and $D \sim 10^{-12}$ m^2/s, respectively.

The source of ions in the bulk liquid crystal, in the absence of fields, is the electrochemical dissociation of impurities or dopants. This is described in the simplest case by the equilibrium reaction.

$$AB \underset{k_r}{\overset{k_d}{\rightleftarrows}} A^{+1} + B^{-1} , \tag{1}$$

where k_d and k_r are the rate constants for dissociation and recombination, respectively. In our doped material, A and B are almost certainly the 8CB itself and the TCNQ dopant; AB is the charge-transfer complex 8CB:TCNQ. However, we have also observed convection in undoped samples of commercial 8CB, in which the ionic species are unknown.

Denoting the number density of the undissociated species AB by c, the number densities of the ions by n_+ and n_-, their mobilities by μ_+ and μ_-, and their diffusion constants by D_+ and D_-, the continuity equations for the number densities are

$$\nabla\cdot(\pm n_\pm \mu_\pm \mathbf{E} - D_\pm \nabla n_\pm + n_\pm \mathbf{v}) + \frac{\partial n_\pm}{\partial t} = k_d c - k_r n_+ n_- , \tag{2}$$

where $\mathbf{v}$ is the fluid velocity and $\mathbf{E}$ is the electric field. The terms in parentheses are the ion fluxes due to migration, diffusion, and convection, respectively. The different signs of the migration term reflects the fact that the two signs of charge migrate in opposite directions. The terms on the right-hand side of Eq. (2) are source terms due to the chemical reaction, Eq. (1). The space-charge density q and electric current density $\mathbf{J}$ are given by

$$q = e(n_+ - n_-) \tag{3}$$

and

$$\mathbf{J} = e(n_+\mu_+ + n_-\mu_-)\mathbf{E} - e(D_+\nabla n_+ - D_-\nabla n_-) + q\mathbf{v} , \tag{4}$$

where e is the magnitude of the electronic charge, so that the continuity equation for charge,

$$\nabla\cdot\mathbf{J} + \frac{\partial q}{\partial t} = 0 , \tag{5}$$

is obeyed. Note that migration contributes to $\mathbf{J}$ even in regions where the space-charge density q is zero, whereas convection contributes only where q is nonzero.

Due to the presence of charges in the film the electric field $\mathbf{E}$ which appears above is not simply the applied field. $\mathbf{E}$ is the self-consistent solution of the above equations and the equations of electrostatics,

$$\nabla\cdot\epsilon\mathbf{E} = q \tag{6}$$

and

$$\nabla\times\mathbf{E} = 0 . \tag{7}$$

Here ϵ is the dielectric permittivity, which for simplicity we treat as a scalar equal to $\epsilon_\perp$, its component perpendicular to the layer normal. Introducing the electric potential ϕ through $\mathbf{E} = -\nabla\phi$, Eq. (6) becomes the Poisson equation,

$$\nabla^2\phi = -q/\epsilon . \tag{8}$$

The flow velocity $\mathbf{v} = (u, v, 0)$, where we assume no flow in the direction perpendicular to the film plane, is governed by the Navier-Stokes equations

$$\rho\left[\frac{\partial \mathbf{v}}{\partial t} + (\mathbf{v}\cdot\nabla)\mathbf{v}\right] = -\nabla P + \eta\nabla^2\mathbf{v} + q\mathbf{E} , \tag{9}$$

where ρ is the mass density and P is the pressure. In general the viscosity is anisotropic but the layer structure of the smectic and the thinness of the film restrict the flow so that the viscosity η is essentially equal to η_3, the viscosity component related to shears within the layer planes. In 8CB, $\eta_3 \approx 0.1$ kg/ms [14,36] and $\rho = 1.0\times10^3$ kg/m^3 [37]. The incompressibility of the flow gives

$$\nabla\cdot\mathbf{v} = 0 . \tag{10}$$

We now consider the appropriate boundary conditions on the dynamical variables $\mathbf{v}$, $n_\pm$ and ϕ. At the electrodes, rigid boundary conditions apply and $\mathbf{v} = 0$. Equation (10) leads to an additional boundary condition on the derivatives of $\mathbf{v}$, i.e., $\partial u/\partial x = \partial v/\partial y = 0$ at the electrodes.

The free surfaces have free-slip boundary conditions, $\hat{\mathbf{k}}\cdot\mathbf{v}=0$, where $\hat{\mathbf{k}}$ is the unit normal to the surface. Since the experiments indicate that the position of the free surface is unaffected by the flow, we can neglect any surface-tension effects.

If we assume an infinitely long film, no boundary conditions are needed for the ends. The ion densities $n_\pm$ are zero in the empty space outside the film, but the fields are not; this aspect of the system prevents it from being treated as completely two dimensional. The film suspended between the wire electrodes constitutes a capacitor partly filled with dielectric, with discontinuities in the permittivity ϵ at the free surfaces of the film, so the fields there are subject to the matching conditions

$$\hat{\mathbf{k}}\cdot(\epsilon\mathbf{E}_i-\epsilon_0\mathbf{E}_o)_f=0 \tag{11}$$

and

$$\hat{\mathbf{k}}\times(\mathbf{E}_i-\mathbf{E}_o)_f=0\ , \tag{12}$$

where ϵ_0 is the permittivity of free space, and $\mathbf{E}_i$ and $\mathbf{E}_o$ are the fields inside and outside the film, respectively. The subscript f denotes values at the free surfaces of the film.

Denoting the applied voltage by ϕ_0, the boundary conditions on ϕ at the anode (a) and cathode (c) are

$$\phi_a=+\phi_0/2\ , \tag{13a}$$

$$\phi_c=-\phi_0/2\ , \tag{13b}$$

while at the free surfaces the flux of each ion across the surface is zero. These fluxes are given by the quantities in parentheses in the continuity equation, Eq. (2). Thus

$$\hat{\mathbf{k}}\cdot(\pm n_\pm\mu_\pm\mathbf{E}_i-D_\pm\nabla n_\pm+n_\pm\mathbf{v})_f=0 \tag{14}$$

at the free surfaces. The convection term $\hat{\mathbf{k}}\cdot\mathbf{v}$ is zero because of the boundary conditions on $\mathbf{v}$. The resulting conditions on $n_\pm$ at the free surfaces,

$$\pm n_\pm\hat{\mathbf{k}}\cdot(\mu_\pm\mathbf{E}_i)_f=\hat{\mathbf{k}}\cdot(D_\pm\nabla n_\pm)_f\ , \tag{15}$$

describe the formation of charged diffusion layers near the free surfaces having a characteristic thickness equal to the Debye screening length $\lambda_D=[\epsilon D/(n_+\mu_++n_-\mu_-)]^{1/2}$. These layers play an important role in producing the convection we are studying, since they are regions of nonzero space charge; it is on these regions that the electric field acts to drive the flow through the body force term in Eq. (9). For our films, λ_D can be of order the film thickness, so these charged layers may extend a considerable way into the film.

Space-charge layers can also be produced at the electrodes. The boundary conditions on $n_\pm$ at the electrodes may involve the creation or destruction of ions due to electrochemical reactions which can be important at dc or very low frequency [12,24,38]. The flux of ions of each type entering or emerging from each electrode is given by an expression similar to Eq. (14), but with $\hat{\mathbf{k}}$ the unit normal to the electrode and with a flux which may be nonzero:

$$\hat{\mathbf{k}}\cdot(\pm n_\pm\mu_\pm\mathbf{E}-D_\pm\nabla n_\pm+n_\pm\mathbf{v})_{a,c}=F^\pm_{a,c} \tag{16}$$

at the electrodes. Again, the convection term is zero due to the boundary conditions on $\mathbf{v}$. The fluxes $F^\pm_{a,c}$ are in principle calculable from a knowledge of the electrochemical reactions in the system. The diffusion term in Eq. (16) allows for the variation of $n_\pm$ inside diffusion layers on the electrodes; the thickness of these layers is also of order λ_D provided that the electrochemical reactions do not violate electroneutrality.

Diffusion across the width of the film takes place over time scales of order $\tau_d=d^2/D\approx10^6$ s for $d=1$ mm. This is much longer than the duration of any of the experiments, and so diffusion on the scale of d can be neglected. Diffusion over smaller distances, of order s or λ_D, is, however, important, since it leads to the formation of the diffusion layers at the free surfaces and the electrodes, and it is these regions of charge separation that interact with the field to cause the convection. If diffusion is neglected in Eq. (16) [30,39], the boundary conditions on the fluxes are equivalent to simply specifying the values of n_+ and n_- on each electrode.

The boundary conditions on ϕ and $n_\pm$ at the electrodes independently specify the voltage across and the current through the film. The relation between the two, which is non-Ohmic in general, depends on the details of the electrochemistry. The simplest case, which occurs at low voltages, is that in which the electrochemical processes do not greatly affect the diffusion layers on the electrodes. In this case electroneutrality is not significantly violated and the interface behaves like an Ohmic contact. At higher voltages, the current is limited by the rate of diffusion of carriers through the layers, and saturation occurs. At still higher voltages, the electrical neutrality of the bulk liquid is violated and the electrode can act as an injector of charge [38,40]. In all of these cases, detailed analysis of the electrochemistry can be avoided by treating the fluxes at each electrode as independent parameters [30].

In summary, the equations describing our system are the continuity equations for the number densities $n_\pm$ [Eq. (2)], the Poisson equation [Eq. (8)], the Navier-Stokes equations [Eq. (9)], and the incompressibility condition [Eq. (10)], along with the appropriate boundary conditions on $n_\pm$, ϕ and $\mathbf{v}$ at the electrodes and the free surfaces.

Solution of these equations is unfortunately rather difficult. The equations simplify somewhat in the limit of fast chemical reactions and small charge separations, as discussed in Appendix A. In this limit the film can be treated as a uniform conductor of conductivity $\sigma=e(\mu_+n_++\mu_-n_-)$, and the equation of charge continuity becomes

$$\frac{\partial q}{\partial t}+\nabla\cdot(\sigma\mathbf{E}+q\mathbf{v}-D\nabla q)=0\ , \tag{17}$$

where we have set $D_+=D_-=D$ for simplicity.

The hydrodynamic part of the problem, Eqs. (9) and (10), could be simplified by treating the film as a two-dimensional liquid. The body force term in the Navier-Stokes equations would then involve a three-dimensional electric field acting on a two-dimensional charge distribution, so the electromagnetic part of the problem remains

three dimensional. Nonetheless a solution of this system of equations should be possible. We do not attempt one here, but use the equations as an aid to understanding the behavior of the convecting films.

III. RESULTS

A. Current-voltage characteristics of the films

When convection is present in a film, charge transport is assisted by flow, and the effective resistance of the film decreases. The onset of convection is thus marked by a change in slope on a plot of the current through the film as a function of the applied voltage. In addition, current-voltage measurements can be used to extract information about the total charge and degree of charge separation in the film. These properties affect the extent to which the film can be modeled as a uniform conductor.

The currents involved are very small, on the order of 10–100 pA; to measure them we used a current-to-voltage converter based on the AD549 electrometer operational amplifier with a Victoreen 102 GΩ feedback resistor. Guard electrodes and shielded triaxial cables were used to minimize leakage currents.

Figure 3(a) is a plot of current versus applied voltage for a typical film. This plot was made by applying a very low frequency ($\sim$4 mHz) sine wave voltage to the film, and waiting several periods for the initial transients to die away. The small hysteresis loop evident in the figure is due to the capacitance of the film and stray capacitances in the electrometer which make the current slightly out of phase with the applied voltage.

Below the onset of convection the film behaves ohmically. The increased charge transport due to convection appears in Fig. 3(a) as an abrupt increase in the slope. Figure 3(b) shows the same data with a linear fit to the data for $V < V_c$ subtracted. The kinks signaling the onset of flow occur at the same point for increasing and decreasing voltages, indicating that the bifurcation is forward and confirming the visual observations reported previously [8–10]. Above V_c, the convection current carried by the film is roughly linear in $V - V_c$.

Determining V_c from the current-voltage curves is potentially more accurate than the visual method described in detail in Ref. [10], for frequencies close to dc. However, this method is not useful for frequencies above about 100 mHz, where the capacitive effects which cause the hysteresis in Fig. 3(a) make the kink in the current-voltage relation at the critical voltage difficult to locate.

While precautions were taken to exclude leakage currents through cable insulation, etc., it was not possible to eliminate currents through the excess liquid crystal which wets the film holder around the edges of the film. This wetting layer usually contains more material than the film itself. The current through this layer can be estimated by measuring the conductance of films of different lengths but the same width and thickness, in the Ohmic regime below the onset of convection. The properties of the smectic films make it possible to increase the film length without thickness change by slowly moving the wipers to draw material out of the wetting layer. Pro-

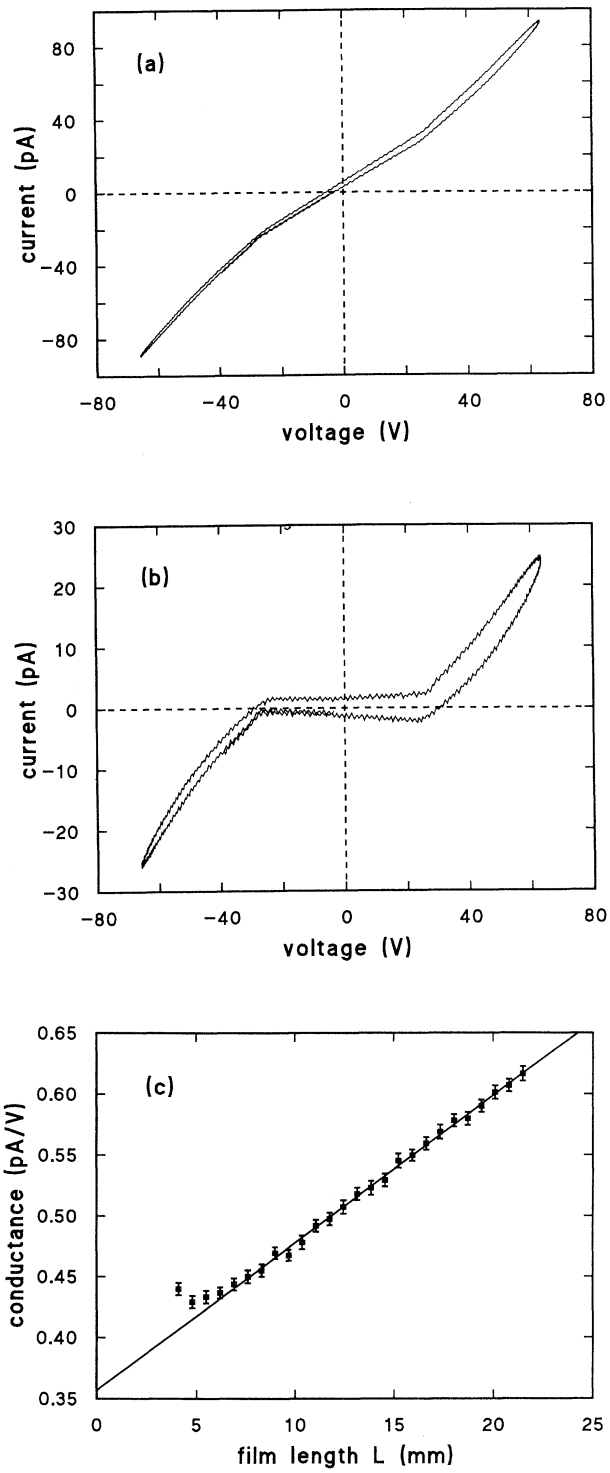

FIG. 3. (a) The IV curve of a typical film. The small hysteresis loop is due to capacitive effects. (b) The same data with a linear fit to the data with $V < V_c$ subtracted, so that only the extra current due to convection remains. The transition to convection occurs at the same voltage for increasing and decreasing voltages. (c) The conductance of a film with a constant thickness of 122±2 layers and width 2.1±0.1 mm, as a function of its length L. The nonzero intercept is a measure of the current flowing around the edges of the film.

vided this process does not significantly reduce the volume of the wetting layer, the leak path can be modeled as an L-independent conductance G_l in parallel with the conductance of the film. The film itself may be modeled as a slab with effective conductivity σ_{eff} and conductance $G_f=\sigma_{\text{eff}}Ls/d$, so that the total conductance

$$G_{\text{tot}}=G_l+\left[\frac{\sigma_{\text{eff}}s}{d}\right]L \tag{18}$$

is linear in L. Figure 3(c) shows the conductance determined from the slopes of current-voltage curves below the onset of convection, as a function of L, for a film of 122 ± 2 layers thickness. The intercept at $L=0$ indicates that for this particular film, about half of the total current when $L=20$ mm was due to leakage around the ends of the film.

Below the onset of convection the film behaves Ohmically. The slope of the line in Fig. 3(c) gives an effective conductivity $\sigma_{\text{eff}}=(6.6\pm0.3)\times10^{-8}\ \Omega^{-1}\text{m}^{-1}$. This effective conductivity is an average over the entire film. The *local* conductivity

$$\sigma=e(\mu_+n_++\mu_-n_-) \tag{19}$$

may vary with position due to the rearrangement of charge by the applied field, electrode reactions, or, for $V>V_c$, convection. We argue in Appendix A, however, that $\sigma_{\text{eff}}/\sigma=1$ to a very good approximation in our experiments.

From the measured value of σ_{eff} we can calculate the screening length λ_D; we find $\lambda_D\approx30$ nm, or approximately ten smectic layers. We observed convection in films with $2\lesssim s/\lambda_D\lesssim15$. Thus although the film is a conductor, it is not electrically neutral over a substantial fraction of its thickness due to the screening layers at the nearby free surfaces.

Any additional charge due to injection at the electrodes would be superimposed on that due to the charged diffusion layers. The Ohmic behavior of the film below V_c shows no sign of the saturation expected if the current were diffusion limited. One cannot conclude from this alone, however, that injection is not present at dc [38]. In more weakly doped and undoped samples, the current-voltage curves, which were for those samples rather irreproducible, do show significant nonlinearity [8] which may be due to injection effects. However, our previous results with ac fields and blocked electrodes [9,10] suggest that, at least for those cases, injection is not *necessary* for convection to occur, the charged diffusion layers alone are sufficient to drive convection.

B. Pattern wavelength

The dependence of the pattern wavelength at onset on the frequency of the applied field was discussed briefly in Ref. [10] and above. The frequency ω' at which the pattern wavelength starts to decrease depends on both the width and thickness of the film, as illustrated in Fig. 4, which shows the reduced wavelength λ/d at onset as a function of frequency for several films of fixed width and a range of thicknesses. This behavior can be interpreted

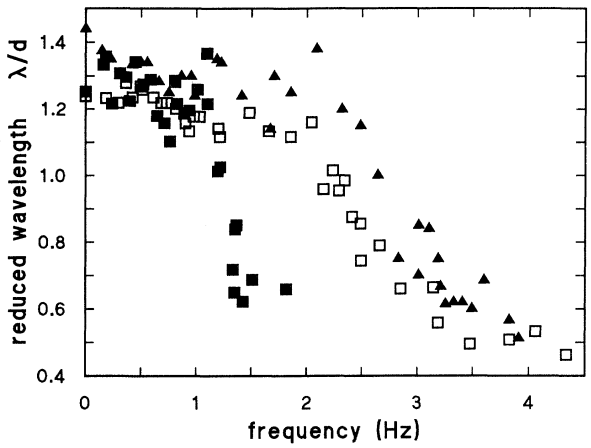

FIG. 4. The reduced wavelength λ/d vs frequency for films of width 2.20 mm and three different thicknesses: ■, 68 layers; □, 102 layers; △, 143 layers.

as a consequence of the finite relaxation time of the space-charge distribution in the film.

The relaxation time of a region of space charge in a three-dimensional conductor is $\tau_3=\epsilon/\sigma$, which for our material is on the order of 10^{-3} s. However, our film can only be treated as a bulk liquid on length scales $\lesssim s$, while the convection involves charge separations on the scale of $d\gg s$; on this length scale the film may be treated as a two-dimensional conducting sheet with a surface conductivity proportional to s. A charge distribution of characteristic size δ in such a sheet relaxes with a characteristic time [17,41]

$$\tau_2(\delta)=\frac{\epsilon_0\delta}{\pi s\sigma}\ , \tag{20}$$

which is a factor of 10^2 to 10^3 times slower than τ_3, and is therefore comparable to the period of the applied field used in our experiments. If the frequency ω of the applied field is such that $\omega\tau_2(\delta)\gg1$, there will be insufficient time for the charge distribution to develop structure with a length scale of order δ. In particular, a pattern with wavelength λ will be accompanied by a charge distribution with scale $\delta\sim\lambda\sim d$. It follows that below a cutoff frequency

$$\omega'=\tau_2^{-1}(d)=(\pi\sigma/\epsilon_0)s/d\ , \tag{21}$$

the pattern can develop as it does at dc, with $\lambda=1.3d$. We show in Fig. 5 a plot of ω' vs s/d; the predicted proportionality is confirmed within the experimental scatter.

For $\omega\gtrsim\omega'$, the oscillating charge distribution at onset can only sustain patterns with wavelength $\lambda\lesssim\lambda(\omega)$, where

$$\frac{\lambda(\omega)}{d}\approx\frac{\omega'}{\omega}\ . \tag{22}$$

Above ω' the wavelength deceases more rapidly than predicted by the simple argument leading to Eq. (22). A more detailed theoretical analysis of the system is required to explain the details of the wavelength selection processes taking place in this parameter range.

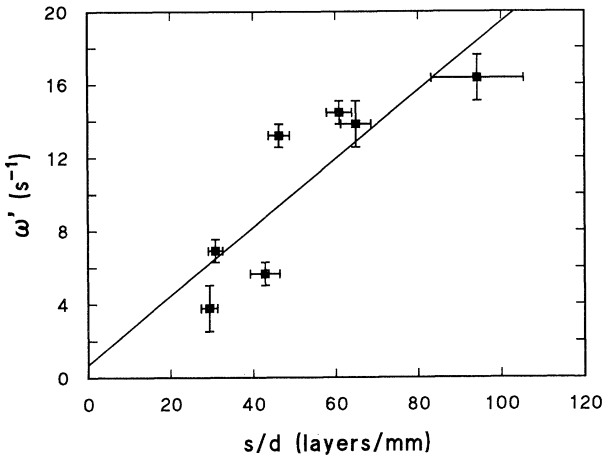

FIG. 5. The cutoff frequency ω' at which the pattern wavelength starts to decrease, as a function of the ratio of film thickness to width. The line is a fit to the plotted data.

C. The velocity field

The two-dimensional nature of the velocity field makes it particularly suited to quantitative flow visualization. In this section we present measurements of the velocity field for a film at dc, for voltages between V_c and the onset of unsteady flow. We measured both x and y components of the velocity over the whole width of the film for a three-vortex-long section near the midpoint. From these data it is possible to determine the harmonic content of the flow pattern and to study the growth of the harmonic components as the voltage is increased above onset.

The velocities were obtained from analysis of time-exposed photographs of the flowing films with the flow visualization particles illuminated by a laser beam chopped at a known frequency. A typical such photograph is shown in Fig. 6(a). The positions of the end points of the streaks were digitized, and several adjacent streaks were used to find each velocity vector and an estimate of its uncertainty. Figure 6(b) is a vector plot of the velocity data obtained in this way from the photograph in Fig. 6(a).

The x and y components of the velocity field were fitted to the first few terms of an expansion in a set of orthogonal functions consistent with the rigid boundary conditions on the flow at the electrodes, the symmetry of the vortex pattern, and the incompressibility condition, Eq. (10). Both x and y components of $\mathbf{v}$ were simultaneously fitted by minimizing the quantity

$$\chi^2=\sum_n \left[\left[\frac{u_n-u(x_n,y_n)}{\sigma_{u_n}} \right]^2 + \left[\frac{v_n-v(x_n,y_n)}{\sigma_{v_n}} \right]^2 \right], \tag{23}$$

where $u_n \pm \sigma_{u_n}$ and $v_n \pm \sigma_{v_n}$ are the measured velocity components at position (x_n,y_n). $u(x,y)$ and $v(x,y)$ are given by the expansions

$$u(x,y)=\sum_{i,j} B_{ij} M_i(y) \frac{\sin[(2j-1)p(x-x_0)}{(2j-1)p} \tag{24}$$

and

$$v(x,y)=\sum_{i,j} B_{ij} C_i(y) \cos[(2j-1)p(x-x_0)] . \tag{25}$$

where $M_i(y)$ and the Chandrasekhar function [42] $C_i(y)$ are defined in Appendix B. $p=2\pi\lambda/d$ is the pattern wave number in the x direction, B_{ij} are the mode amplitudes, and x_0 is an arbitrary origin. These expansions are derived in Appendix B. A standard Levenberg-Marquardt nonlinear minimization method [43] was used to minimize χ^2. Each fit involved about 400 measured velocity components at scattered locations; that is, the data were not interpolated onto a grid before fitting.

Just above V_c, the pattern is very well described by a single mode, that is, only B_{11} is significantly different from zero. As the voltage is increased, higher modes become significant; just below the appearance of unsteady flow a satisfactory fit requires two modes in the y direction and three in the x direction, i.e., $B_{ij} \neq 0$ for $i=1,2$ and $j=1,2,3$.

Figures 7(a)–7(c) and 8(a)–8(c) show fits to components of the velocity just above V_c and just below the appearance of unsteady flow, respectively. Since the ve-

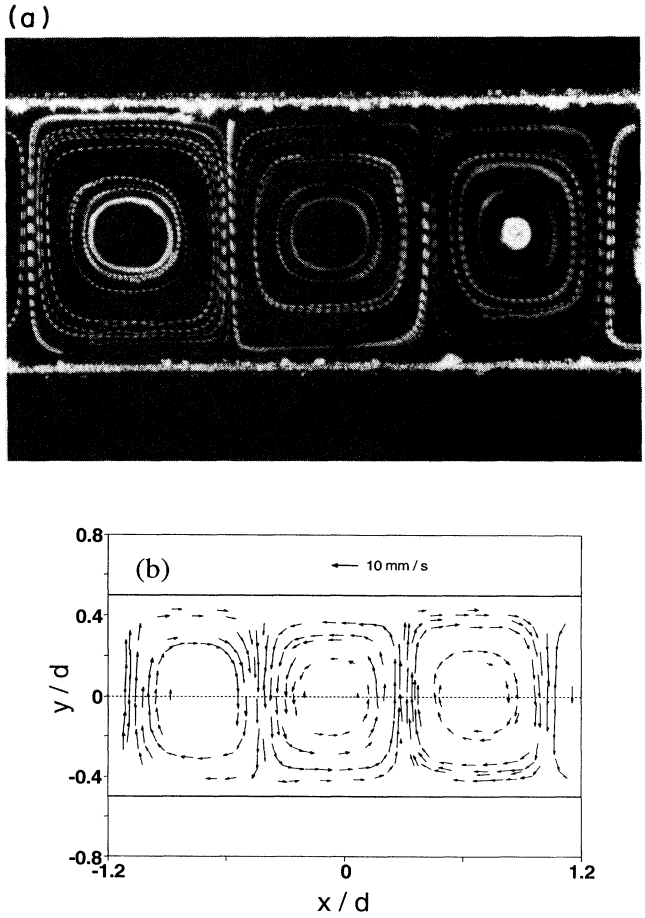

FIG. 6. (a) A streak photograph of the convection pattern close to the onset of unsteady flow. (b) The vector velocity data extracted from (a).

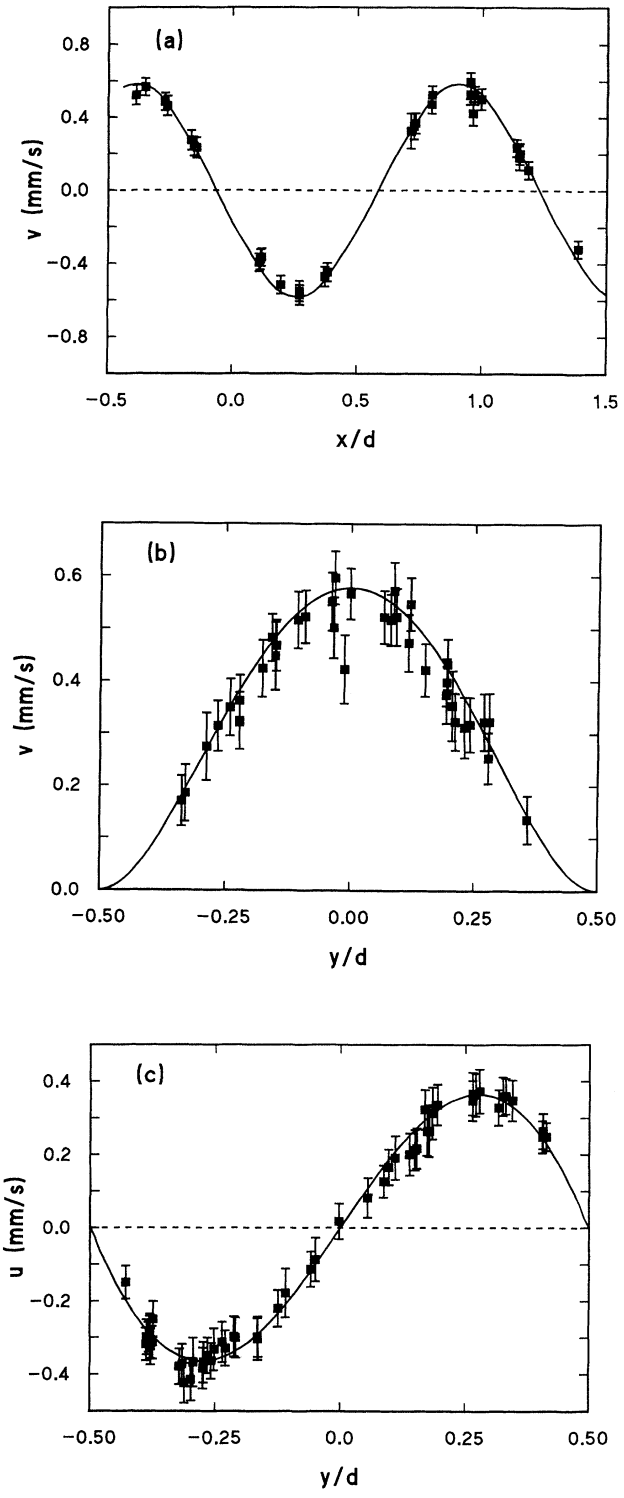

FIG. 7. The fit to the measured velocity field just above the onset of convection using the expansions (24) and (25). Since the fit is two-dimensional, the data from a narrow strip are compared to the fit along the midline of the strip. (a) v vs x/d along the line $y=0$. (b) v vs y/d on the boundary between two vortices. (c) u vs y/d on a line cutting through the center of a vortex. In each case the flow is well described by the lowest mode of the expansions.

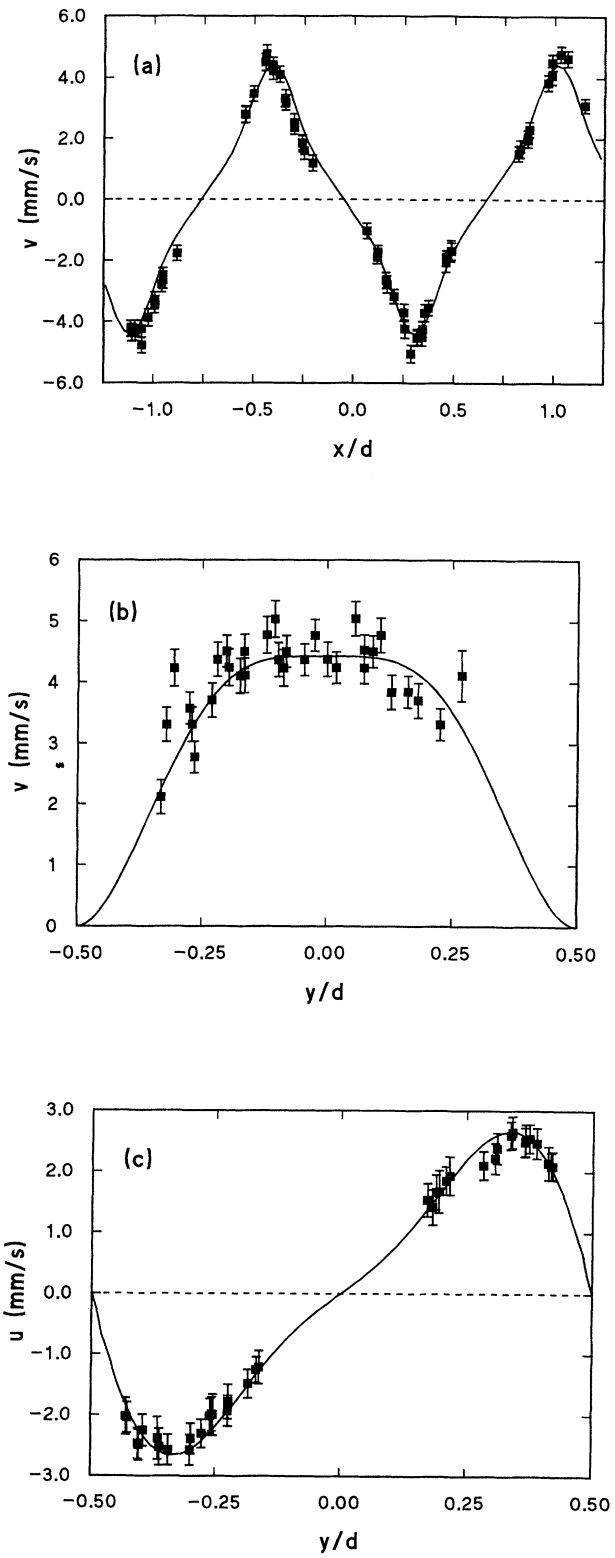

FIG. 8. The fit to the measured velocity field just below the onset of unsteady flow. (a)–(c) show the fit and data along the same lines as in Fig. 7. The presence of higher modes in the flow pattern is evident; the flow tends to become concentrated around the peripheries of the vortices.

locity data are obtained from the photographs at scattered (x,y) points, we have shown the fit along certain lines of symmetry of the flow pattern, together with data falling within a narrow strip around the lines. We emphasize that the fits were to both components of the complete two-dimensional velocity field simultaneously. The figures show only one line of the fit and a small fraction of the data used to obtain the full fit. The presence of higher modes well above onset is evident from Fig. 8.

The variation of the fitted mode amplitudes with the applied voltage is shown in Figs. 9(a) and 9(b). Figure 9(a) shows the behavior of the amplitudes B_{1j}, and the B_{2j} are shown in Fig. 9(b). The data indicate that the flow velocity grows smoothly from zero at the onset of convection. Figure 10 shows the data for the B_{1j} plotted against the dimensionless stress parameter $\epsilon=(V/V_c)^2-1$.

In analogy with the analysis of velocity fields measured for Rayleigh-Bénard convection [44] and Taylor vortex flow [45,46], we expect the amplitudes B_{1j} to behave close to the bifurcation as $\tilde{\epsilon}^{j/2}$, where $\tilde{\epsilon}$ is an appropriate dimensionless stress parameter. Here we take $\tilde{\epsilon}=\epsilon$.

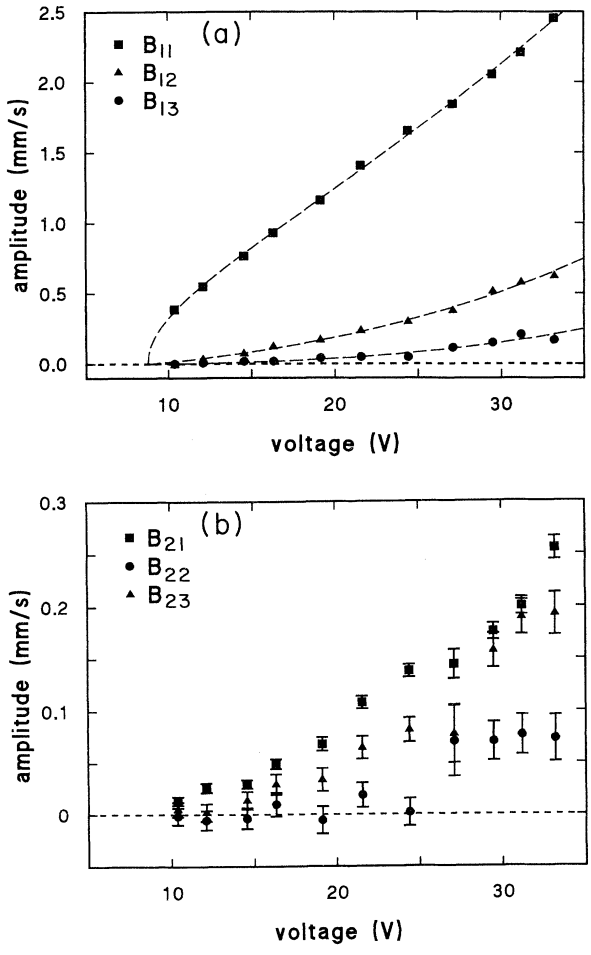

FIG. 9. The amplitudes B_{ij} as a function of applied voltage. (a) B_{1j}. The dashed lines are fits to Eq. (26) discussed in the text. (b) The higher-order amplitudes B_{2j}.

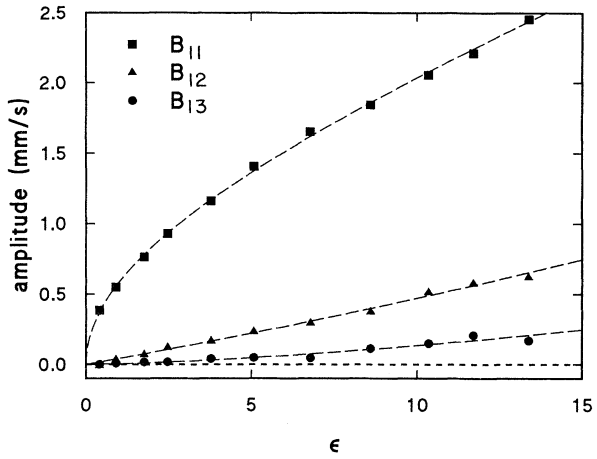

FIG. 10. The amplitudes B_{11}, B_{12}, and B_{13} vs the dimensionless stress parameter $\epsilon=(V/V_c)^2-1$. The dashed lines are the same fits shown in Fig. 9(a).

Since our data cover a fairly large range of ϵ above the bifurcation, higher-order corrections to this behavior are also expected to be significant [45,46]. We therefore fitted our data for B_{1j} to the functions

$$B_{1j}=a_j\epsilon^{j/2}(1+b_j\epsilon)\ , \tag{26}$$

with a_j,b_j $(j=1,2,3)$ and V_c free parameters. Preliminary fits to all three sets of amplitude data indicated that b_3, and any higher-order terms, were statistically insignificant. Fixing b_3 to zero and performing a weighted fit with the remaining six parameters free gives

$$B_{11}=(0.576\pm0.016)\epsilon^{1/2}[1+(0.012\pm0.001)\epsilon]\ , \tag{27}$$

$$B_{12}=(0.042\pm0.004)\epsilon[1+(0.013\pm0.010)\epsilon]\ , \tag{28}$$

$$B_{13}=(0.0043\pm0.0005)\epsilon^{3/2}\ , \tag{29}$$

with $V_c=8.75\pm0.13$ V. These fits are shown as dashed lines in Figs. 9(a) and 10, and describe the data well. The value of V_c found in this way is consistent with that found from visual observations of the onset of flow [10].

IV. DISCUSSION AND CONCLUSION

We have investigated some features of electrically driven convection in a thin film of smectic-A liquid crystal. The submicrometer thickness of the film makes this a delicate convecting system: from our estimate of the charge density we find that an excess charge of only $10^7 e/\text{mm}^2$ and an applied voltage of order 10 V is sufficient to generate flow velocities of approximately 10 mm/s.

Measurements of the current through the film show no hysteresis at onset, supporting our earlier visual observations that the bifurcation to convection is forward [8–10]. The same conclusion can be drawn from our direct measurements of the velocity field. We were able to fit the amplitudes of the various modes in the pattern to an expansion in powers of ϵ of the form used to de-

scribe other systems that display a forward bifurcation, using $\epsilon=(V/V_c)^2-1$. Several spatial Fourier modes are present in the pattern when, at voltages around $5V_c$, a transition to unsteady flow occurs. We were unable to characterize this unsteady flow quantitatively using our simple flow visualization technique.

Under ac driving voltages, the pattern wavelength at onset decreases above a certain frequency. This behavior can be interpreted in a straightforward way as a consequence of driving the film at frequencies close to the inverse of the charge relaxation time. Because of the restricted geometry of the film, this time is a factor of $s/d\sim 10^3$ slower than the bulk relaxation time.

Several future experiments suggest themselves. Interesting behavior is expected in films with thicknesses near the Debye screening length. This can be varied by changing the dopant concentration in the liquid crystal. The regime of unsteady flow remains unexplored; a better probe of the flow velocity, such as laser doppler velocimetry, is needed to understand this region. Studies of the stability boundaries of the flow in the voltage–wave-number plane, and of wavelength selection would be interesting—the wave number can be altered experimentally by slowly moving one of the wipers while the film is convecting. Finally, the experiments could be repeated using a smectic-C material; in this case a coupling of the flow to the molecular orientation is expected [11,12,19]. It would then be possible to visualize the flow by studying the light transmitted through a film placed between crossed polarizers, instead of using suspended particles.

ACKNOWLEDGMENTS

We thank Guenter Ahlers for helpful comments on this manuscript. This research was supported by the Natural Sciences and Engineering Research Council of Canada, and by the province of Ontario through the Ontario Laser and Lightwave Research Center.

APPENDIX A

In this appendix we consider the conductivity of the film in the experimentally relevant case of fast chemical reactions, and argue that the film can be treated in this case as a uniform conductor. The effective conductivity measured in Sec. III A is an average over the whole film, while the local conductivity given by Eq. (19) may vary in space. To compare these two quantities we use indirect estimates of the carrier densities $n_\pm$ based on the measured values of the effective conductivity and convective contribution to the current discussed above.

For an applied voltage of $\phi_0=0$, the system is in thermodynamic equilibrium, so the time derivatives and fluxes in Eq. (2) are zero and $n_\pm$ satisfy

$$k_d c = k_r n_+ n_- \ . \tag{A1}$$

Since the film is everywhere electrically neutral when $\phi_0=0$, the equilibrium number densities of the ions are

$$n_+ = n_- = \sqrt{k_d c/k_r} = n_{\rm eq} \ . \tag{A2}$$

We assume that the dissociation of charge-transfer complexes is weak so that $c \gg n_\pm$, and that c is uniform in time and space throughout the film. For small applied voltages, we expect that $n_+ \approx n_- \approx n_{\rm eq}$. Then the liquid can be described by a uniform effective conductivity given by

$$\sigma_{\rm eff} = 2e n_{\rm eq} \mu \ , \tag{A3}$$

where we have put $\mu=\mu_+=\mu_-$. Using the typical value of $\mu\sim 10^{-10}$ m^2/s given in Sec. II, and the measured value of $\sigma_{\rm eff}$, we find $n_{\rm eq}\sim 10^{22}$ m^{-3}.

Next we can get a crude estimate of the degree of charge separation—i.e., the magnitude of q—when the film is convecting. As shown in Fig. 3(b), convection produces an excess current of order 10 pA. If we assume $q=q_0\sin(2\pi x/\lambda)$ and $v=v_0\sin(2\pi x/\lambda)$, take as dimensions $L=10$ mm, $s=0.3$ μm, and $\lambda=2$ mm, and, using Fig. 7, take $v_0=1$ mm/s, we get this current if $q\sim 7$ C/m^3, or of order $10^{20}e$/m^3.

Finally, we can estimate the rate of the dissociation/recombination reactions that generate the charges in the film. Suppose that an excess number of dissociated pairs is produced in a region. In the absence of any ion flux from outside the region, the charge distribution will relax by recombination with a characteristic time [47] $\tau_r=(k_r n_{\rm eq})^{-1}$. The rate constant k_r may be estimated from Langevin's formula [30,47] to be $k_r\approx e\mu/\epsilon$, so $\tau_r\sim 10^{-3}$ s. Thus on the time scale of our experiments the dissociation/recombination reactions can be considered infinitely fast, so that

$$n_+ n_- = n_{\rm eq}^2 \tag{A4}$$

and the source term on the right-hand side of Eq. (2) is always zero. In this approximation, it is easy to show using Eqs. (19) and (A3) that the local conductivity and the space-charge density are related by

$$\sigma = (\sigma_{\rm eff}^2 + \mu^2 q^2)^{1/2} \ . \tag{A5}$$

Using the estimates of $n_{\rm eq}$ and q discussed above, we find

$$\frac{\sigma}{\sigma_{\rm eff}} - 1 \approx 10^{-4} \ , \tag{A6}$$

so that the film is well described as a conductor with a uniform conductivity $\sigma_{\rm eff}$.

APPENDIX B

The flow velocity is governed by the equations and boundary conditions presented in Sec. II above. Taking the film to be infinitely long in the x direction, we can expand the x dependence of $\mathbf{v}=(u,v,0)$ in terms of sines and cosines in x. For the y dependence we use the Chandrasekhar functions [42]

$$S_m(y) = \frac{\sinh(\beta_m y)}{\sinh(\beta_m/2)} - \frac{\sin(\beta_m y)}{\sin(\beta_m/2)} \tag{B1}$$

and

$$C_m(y) = \frac{\cosh(\alpha_m y)}{\cosh(\alpha_m/2)} - \frac{\cos(\alpha_m y)}{\cos(\alpha_m/2)} \ , \tag{B2}$$

which satisfy the experimentally appropriate boundary conditions

$$C_m(\pm\tfrac{1}{2})=\frac{dC_m(\pm\frac{1}{2})}{dy}=S_m(\pm\tfrac{1}{2})=\frac{dS_m(\pm\frac{1}{2})}{dy}=0 \tag{B3}$$

at the electrodes. Here α_m and β_m are the mth roots of

$$\tanh(\beta/2)-\tan(\beta/2)=0 \tag{B4}$$

and

$$\coth(\alpha/2)-\cot(\alpha/2)=0\ . \tag{B5}$$

Measuring distance in units of d we can write down expansions for u and v:

$$u(x,y)=\sum_{k,j} A_{kj}S_k(y)\sin[(2j-1)p(x-x_0)]\ , \tag{B6}$$

$$v(x,y)=\sum_{i,j} B_{ij}C_i(y)\cos[(2j-1)p(x-x_0)]\ . \tag{B7}$$

The coefficients A_{kj} and B_{ij} are related by

$$A_{kj}=\frac{1}{(2j-1)p}\sum_i B_{ij}\left[\frac{8\alpha_k^2\beta_i^2}{\alpha_k^4-\beta_i^4}\right]\ . \tag{B8}$$

This expression results from imposing the incompressibility condition, Eq. (10), on Eqs. (B6) and (B7), equating coefficients, and expanding $\partial C_i(y)/\partial y$ in terms of $S_k(y)$. The term in large parentheses in Eq. (B8) is the matrix element of the expansion, which can be found by several integrations by parts, as described by Chandrasekhar [42].

Substituting Eq. (B8) into Eq. (B6) and rearranging gives Eqs. (24) and (25), with

$$M_i(y)=\sum_k \frac{8\alpha_k^2\beta_i^2}{\alpha_k^4-\beta_i^4}S_k(y)\ . \tag{B9}$$

In restricting the expansions to include only odd harmonics in x, we have assumed that adjacent vortices have a reflection symmetry, i.e., that

$$u(x+\lambda/2,y)=-u(x,y) \tag{B10}$$

and

$$v(x+\lambda/2,y)=-v(x,y)\ . \tag{B11}$$

This assumption reduces the number of parameters in our fits, but prohibits any asymmetry between anode-to-cathode and cathode-to-anode flows that may arise due to, for example, unipolar injection of charge at one electrode. Our data show no evidence for such asymmetry; this is consistent with our other observations that the bifurcation to convection is forward.

To fit our data, we restrict the i and j sums in Eqs. (24) and (25) to the first few terms. The sum over k in Eq. (B9) is not restricted since it contains no adjustable coefficients, it simply defines a new function of y with index i. This sum converges rather slowly; for large k, the terms behave as k^{-2}. To evaluate the sum to within 10^{-3}, which is more than sufficient for our purposes, about 200 terms must be included.

*Present address: Department of Physics, University of California, Santa Barbara, CA 93106-9530.

[1] G. Ahlers, in *Lectures in The Sciences of Complexity,* edited by D. Stein (Addison, Reading, MA, 1989), p. 175.
[2] F. Busse, in *Hydrodynamic Instabilities and the Transition to Turbulence,* edited by H. L. Swinney and J. P. Gollub (Springer, Berlin, 1984) p. 91.
[3] V. Croquette, Contemp. Phys. **30**, 113 (1989); **30**, 153 (1989).
[4] D. Bensimon, P. Kolodner, C. M. Surko, H. Williams, and V. Croquette, J. Fluid Mech. **217**, 441 (1990).
[5] R. C. DiPrima and H. L. Swinney, in *Hydrodynamic Instabilities and the Transition to Turbulence* (Ref. 2), p. 139.
[6] I. Rehberg, B. Winkler, M. de la Torre Juarez, S. Rasenat, and W. Schöpf, in *Festkörperprobleme/Advances in Solid State Physics 29,* edited by U. Rössler (Vieweg, Braunschweig, 1989), p. 35.
[7] A. Joets and R. Ribotta, J. Phys. (Paris) **47**, 595 (1986).
[8] S. W. Morris, J. R. de Bruyn, and A. D. May, in *Nonlinear Evolution of Spatio-temporal Structures in Dissipative Continuous Systems,* edited by F. Busse and L. Kramer (Plenum, New York, 1990), p. 351.
[9] S. W. Morris, J. R. de Bruyn, and A. D. May, Phys. Rev. Lett. **65**, 2378 (1990).
[10] S. W. Morris, J. R. de Bruyn, and A. D. May, J. Stat. Phys. **64**, 1025 (1991).
[11] P. G. de Gennes, *The Physics of Liquid Crystals* (Clarendon, Oxford, 1979).
[12] L. M. Blinov, *Electro-optical and Magneto-optical Properties of Liquid Crystals* (Wiley, New York, 1983).
[13] J. Prost, Adv. Phys. **33**, 1 (1984).
[14] L. Léger and A. Martinet, J. Phys. (Paris) Colloq. **37**, C3-89 (1976).
[15] R. Pindak and D. Moncton, Phys. Today **35**(5), 57 (1982).
[16] C. Y. Young, R. Pindak, N. A. Clark, and R. B. Meyer, Phys. Rev. Lett. **40**, 773 (1978); R. Pindak, C. Y. Young, R. B. Meyer, and N. A. Clark, *ibid.*, **45**, 1193 (1980).
[17] C. Rosenblatt, R. B. Meyer, R. Pindak, and N. A. Clark, Phys. Rev. A **21**, 140 (1980).
[18] H. Hsiung and Y. R. Shen, Phys. Rev. A **34**, 4303 (1986).
[19] P. E. Cladis, Y. Couder, and H. R. Brand, Phys. Rev. Lett. **55**, 2945 (1985).
[20] Y. Couder, J. Phys. (Paris) **45**, L353 (1984).
[21] Y. Couder and C. Basdevant, J. Fluid Mech. **173**, 225 (1986).
[22] Y. Couder, J. M. Chomaz, and M. Rabaud, Physica D **37**, 384 (1989).
[23] M. Gharib and P. Derango, Physica D **37**, 406 (1989).
[24] R. Cocco, F. Gaspard, and R. Herino, J. Chim. Phys. (Paris) **76**, 383 (1979).
[25] A. J. Leadbetter, J. C. Frost, J. P. Gaughan, G. W. Gray, and A. Mosly, J. Phys. (Paris) **40**, 375 (1979).
[26] M. Born and E. Wolf, *Principles of Optics* (Pergamon, New York, 1980).
[27] C. Rosenblatt and N. Amer, Appl. Phys. Lett. **36**, 432 (1980).

[28] J. C. Lacroix, P. Atten, and E. J. Hopfinger, J. Fluid Mech. **69**, 539 (1975).
[29] P. Atten and J. C. Lacroix, J. Méc. **18**, 469 (1979).
[30] P. Atten, J. Méc. **14**, 461 (1975).
[31] S. Faetti, L. Fronzoni, and P. A. Rolla, J. Chem. Phys. **79**, 1427 (1983).
[32] S. Faetti, L. Fronzoni, and P. A. Rolla, J. Chem. Phys. **79**, 5054 (1983).
[33] J. M. Schneider and P. K. Watson, Phys. Fluids **13**, 1948 (1970).
[34] R. J. Turnbull, J. Phys. D **6**, 1745 (1973).
[35] A. Mircea-Roussel, L. Léger, F. Rondelez, and W. H. de Jeu, J. Phys. (Paris) Colloq. **36**, C1-93 (1975).
[36] R. G. Horn and M. Kléman, Ann. Phys. (Paris) **3**, 229 (1978).
[37] D. A. Dunmur, M. R. Manterfield, W. H. Miller, and J. K. Dunleavy, Mol. Cryst. Liq. Cryst. **46**, 127 (1978).
[38] N. J. Felici, J. Phys. (Paris) Colloq. **37**, C1-11 (1976).
[39] A. T. Pérez and A. Castellanos, Phys. Rev. A **40**, 5844 (1989).
[40] R. Bruinsma and S. Alexander, J. Chem. Phys. **92**, 3074 (1990).
[41] S. Faetti, L. Fronzoni, and P. A. Rolla, J. Phys. (Paris) Colloq. **40**, C3-497 (1979).
[42] S. Chandrasekhar, *Hydrodynamic and Hydromagnetic Stability* (Clarendon, Oxford, 1961).
[43] W. H. Press, B. P. Flannery, S. A. Teukolsky, and W. T. Vetterling, *Numerical Recipes in C* (Cambridge University Press, Cambridge, 1988).
[44] M. Dubois and P. Bergé, J. Fluid Mech. **85**, 641 (1978).
[45] R. M. Heinrichs, D. S. Cannell, G. Ahlers, and M. Jefferson, Phys. Fluids **31**, 250 (1988).
[46] A. Davey, J. Fluid Mech. **14**, 336 (1962).
[47] I. Adamczewski, *Ionization, Conductivity and Breakdown in Dielectric Liquids* (Taylor and Francis, London, 1969).

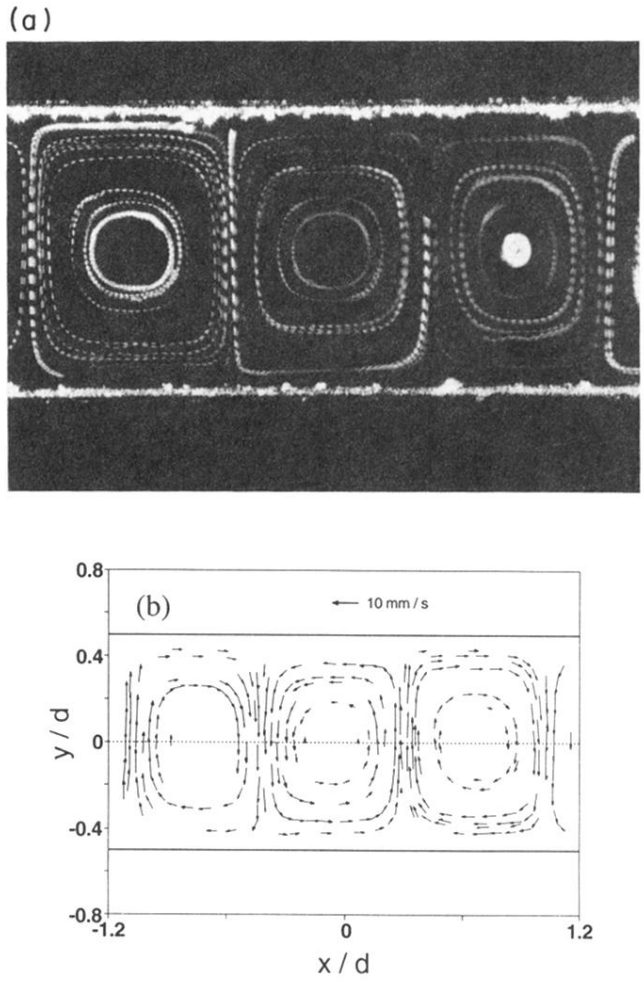

FIG. 6. (a) A streak photograph of the convection pattern close to the onset of unsteady flow. (b) The vector velocity data extracted from (a).